JACS
JOURNAL OF THE AMERICAN CHEMICAL SOCIETY
pubs.acs.org/JACS
Article

Frustrated Interfacial Solvation Enhances Reaction Rates at Acidified Ice Grain Boundaries in Frozen Microdroplets

Runbo Wang,◆ Kuan Luo,◆ Tao Wang,* Yu Wei, Jilun Wang, Le Yang, Wenbo You, Qiuyue Ge, Yangyang Liu, Minglu Ma, Kejian Li, Yuting Lyu, Laurentiu-Gabriel Movila, Xiang Sun, Huiming Bao, Jianmin Chen, Christian George, Norimichi Takenaka, Markku Kulmala, Minbiao Ji,* Liwu Zhang,* and Zhang Lin*

Cite This: J. Am. Chem. Soc. 2026, 148, 37134−37143

Read Online

ACCESS | Metrics & More | Article Recommendations | Supporting Information

ABSTRACT: Ice is ubiquitous in natural environments, yet the interstitial liquid trapped within polycrystalline grain boundaries remains difficult to access, limiting mechanistic understanding of accelerated reactions in ice. Here, we combine cryogenic stimulated Raman scattering microscopy with multivariate curve resolution to visualize and spectroscopically resolve internal constituents of frozen microdroplets. We identify pronounced structural heterogeneity: the entrapped interstitial liquid displays more strongly hydrogen-bonded water signatures than bulk supercooled water, whereas the ice−water interface shows diminished orientational ordering, whereby water hydrogen atoms are less preferentially aligned toward solutes, consistent with frustrated solvation and partial desolvation. Using sulfur dioxide autoxidation as a model reaction, we find that frozen microdroplets exhibit an approximately 20-fold faster apparent oxidation rate than supercooled liquid microdroplets under otherwise comparable conditions. Kinetic analysis and simulations suggest that interfacial frustrated solvation, together with grain boundary acidification, lowers the effective barrier for electron transfer and radical initiation and the associated enhancement of sulfate formation. These findings provide a microscopic link between buried ice−water interfacial structure and low-temperature reaction kinetics, with implications for atmospheric chemistry in cold and mixed-phase environments.

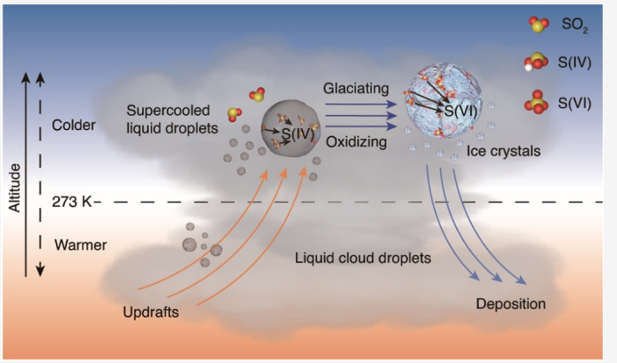

INTRODUCTION

The freezing of aqueous microdroplets is a ubiquitous phase transition[1] governing solute partitioning across atmospheric science,[2] cryobiology,[3] and materials engineering.[4] The solidification of supercooled droplets creates highly confined microenvironments within ice grain boundaries and interstitial junctions.[5,6] The rheology, melting, and electrostatic properties of polycrystalline ice are fundamentally governed by its microscopic structural heterogeneities.[7−9] While surface-sensitive techniques have revealed that the quasi-liquid layer (QLL) on premelted ice exhibits slightly hydrophobic characteristics,[10] hydrogen bond asymmetry,[11] and an electrical double layer,[12] the properties of the deeply buried ice grain boundaries, consisting of interstitial liquid and ice−water interfaces enclosed within them, remain largely unexplored. These deeply buried microenvironments remain inaccessible to surface-specific techniques, while their subtle spectroscopic signatures are overwhelmingly obscured by the bulk ice matrix in conventional ensemble-averaging measurements.

Resolving these hidden internal microstructures is critical, as freezing can accelerate and even trigger new reactions involving compounds excluded by the ice lattice.[13] These reactions have attracted considerable attention in recent years because of their profound significance for both polar environments and green chemistry. While increasing evidence suggests that these accelerated kinetics cannot be solely explained by macroscopic effects like traditional freeze-concentration or pH shifts,[14,15] the fundamental chemical mechanisms driving these reactions remain elusive. Specifically, a critical scientific question persists: how do reactant-solvent interactions within these confined spaces thermodynamically and kinetically alter reaction pathways? Because the true state of the ice−water interface has been a "black box" (as discussed above), the specific solvation structures of reactants and their exact role in lowering electron-transfer energy barriers remain largely unexplored. To bridge this gap between microscopic solvation and macroscopic

Received: June 4, 2026
Revised: August 12, 2026
Accepted: August 13, 2026
Published: August 24, 2026

https://doi.org/10.1021/jacs.6c11450
J. Am. Chem. Soc. 2026, 148, 37134−37143

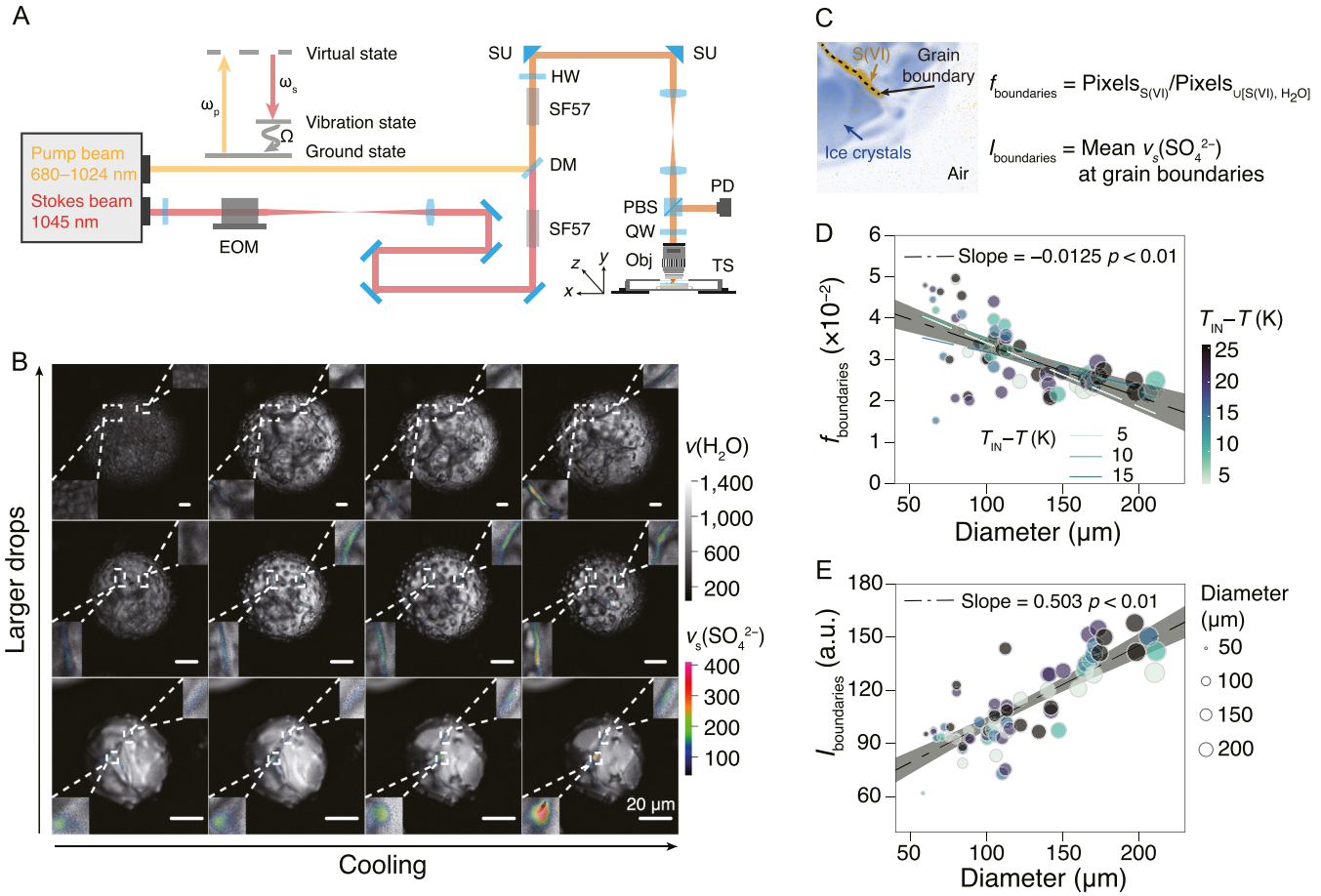

Figure 1. Stimulated Raman scattering imaging of frozen microdroplets. (A) Schematic of the cryogenic stimulated Raman microscopy setup (EOM: electro-optical modulator; DM: dichroic mirror; HW: half-wave plate; SU: scan unit; PBS: polarizing beamsplitter cube; QW: quarter-wave plate; TS: temperature-regulated microscope stage; PD: photodiode) and energy diagram of the SRS process (ω_p: pump photons; ω_s: Stokes photons; $\Omega = \omega_p - \omega_s$). (B) SRS images of frozen microdroplets scanned at the Raman shift of 3420 cm^{-1} $\nu(H_2O)$ (stretching vibration of H_2O) and 985 cm^{-1} $\nu_s(SO_4^{2-})$ (symmetrical stretching vibration of SO_4^{2-}) with different microdroplet diameters (60, 145, and 230 μm) at $T_{IN}-T$ of 0, 5, 10, and 15 K (T_{IN} is the freezing temperature and T is the measurement temperature). Certain regions of solute distribution are magnified and inset. The scale bar represents 20 μm. (C) Composite image of a quarter section of a frozen microdroplet (with a diameter of 60 μm, measured at $T_{IN}-T$ of 10 K), showing $\nu(H_2O)$ (blue) and $\nu_s(SO_4^{2-})$ (yellow) distributions, based on which two parameters can be defined: $f_{boundaries}$ (the fraction of ice grain boundaries) and $I_{boundaries}$ (the intensity of freeze-concentration). (D) $f_{boundaries}$ and (E) $I_{boundaries}$ plotted as a function of microdroplet diameter. Color bar indicates $T_{IN}-T$, and the symbol size is proportional to microdroplet diameter. The black dot-dashed line represents least-squares linear regression fit to the entire data set, and the gray shaded region represents the 95% confidence intervals, with the slope of regression line and probability value (p, obtained by Spearman correlation test) listed alongside. Colored dashed lines represent linear regression fits of $f_{boundaries}$ versus microdroplet diameter at different $T_{IN}-T$.

kinetics, we investigated accelerated sulfur dioxide (SO_2) autoxidation in frozen microdroplets, serving as an ideal model system to decode the fundamental interplay between interfacial confinement and chemical reactivity.

To directly probe these elusive microenvironments and unravel the interfacial solvation dynamics, we employed cryogenic stimulated Raman scattering (SRS) microscopy. By leveraging the high-resolution 3D optical sectioning capability of nonlinear chemical imaging, we tracked the *in situ* microdynamics of individual frozen microdroplets. Coupled with multivariate curve resolution with alternating least-squares (MCR-ALS), this approach allows us to spatially resolve and spectroscopically decouple the distinct vibrational signatures of the interstitial liquid and the ice–water interface from the bulk ice. Kinetic experiments and theoretical calculations further corroborate the elucidated mechanism, highlighting the unique role of ice–water interface and the acidification of ice grain boundaries. The reduced electron-transfer energy may be associated with frustrated solvation of solute molecules at this acidified interface, characterized by multiple orientations of the surrounding water molecules[16] and weakened solute-water and water–water hydrogen bonding. Consequently, this mechanism offers a plausible explanation for the long-standing puzzle of rapid S(VI) formation in cold environments, such as ice fog.[17,18] Looking forward, the frequency of deep convective events and associated freezing processes (*e.g.*, hailstorms) is expected to increase over the next 40–50 years due to climate change.[19] Therefore, the transport of these frozen microdroplets—rich in reaction products—into the lower troposphere represents an unrecognized but critical process relevant to earth science.

RESULTS AND DISCUSSION

Microdynamics of Polycrystalline Ice Structure within Frozen Droplets

We imaged and analyzed the frozen microdroplets with various diameters (58–211 μm) using the setup illustrated in Figure 1A.

https://doi.org/10.1021/jacs.6c11450
J. Am. Chem. Soc. 2026, 148, 37134–37143

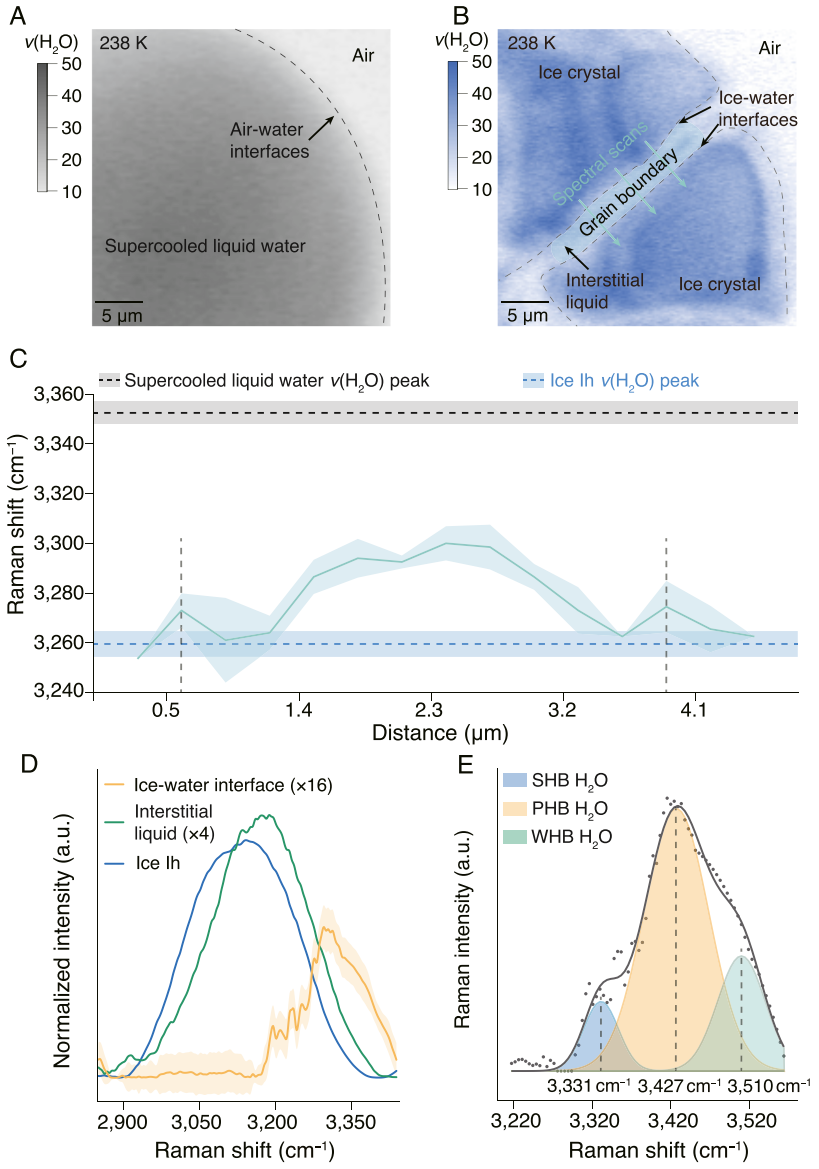

Figure 2. Characterization of ice grain boundaries. (A, B) Composite image of a quarter section of a liquid microdroplet and frozen microdroplet distinguished by $\nu(H_2O)$ intensity (blue). The gray shaded region marks ice grain boundary, where SRS spectral scans were collected from the same direction. (C) Peak frequencies of $\nu(H_2O)$ at different distances from the starting point of scanning. The sea green solid line indicates the mean $\nu(H_2O)$ positions at different distances. The gray and blue lines indicate the mean $\nu(H_2O)$ frequencies for supercooled liquid water and ice Ih (hexagonal water ice), respectively. The shaded area represents one standard deviation. (D) MCR-ALS separated SRS spectra of ice−water interface, interstitial liquid, and ice Ih. The shaded region represents the 95% confidence interval of the extracted interfacial spectrum. (E) SRS spectra of ice−water interface fitted by Gaussian profiles (SHB H_2O: saturated H-bonded H_2O; PHB H_2O: partially H-bonded H_2O; WHB H_2O: weakly H-bonded H_2O). The standard deviations of the peak positions for SHB, PHB, and WHB are 6.0, 2.4, and 10.3, respectively. Symbols denote actual original signal, while the gray solid line depicts the sum of 3 Gaussians.

To investigate the behavior and distributions of solutes in frozen microdroplets, water microdroplets were prepared from a sulfate-containing solution, exploiting both the strong Raman cross section of sulfate and its abundant presence in nature.[20] Microdroplets were sprayed onto a hydrophobic substrate (Text S1 of SI), cooled at a constant rate (1 K min^{-1}), following heterogeneous ice nucleation and complete freezing. SRS signals were generated when pump and Stokes beams temporally and spatially overlapped at the matched Raman frequency (Text S2 of SI). Targeting the vibrational modes of sulfate ($\nu_s(SO_4^{2-})$ at 985 cm^{-1}) and water ($\nu(H_2O)$ within 3000−3500 cm^{-1}) enabled high-resolution imaging of ice grain boundaries within frozen microdroplets with different microdroplet diameters and $T_{IN}-T$ levels, where T_{IN} is the ice nucleation temperature and T (lower than T_{IN}) is the measurement temperature.

The evolution of sulfate signals indicates that freezing concentrates solutes within ice grain boundaries inside the microdroplet, where the solute concentration clearly increases as the temperature decreases (Figure 1B). A detailed imaging analysis of individual microdroplets further elucidates the temperature-induced structural dynamics of polycrystalline ice. Specifically, the morphological evolution of grain boundaries demonstrates that progressive cooling not only contracts grain boundaries but also drives the spatial redistribution of solutes (Figure S2B).

https://doi.org/10.1021/jacs.6c11450
J. Am. Chem. Soc. 2026, 148, 37134−37143

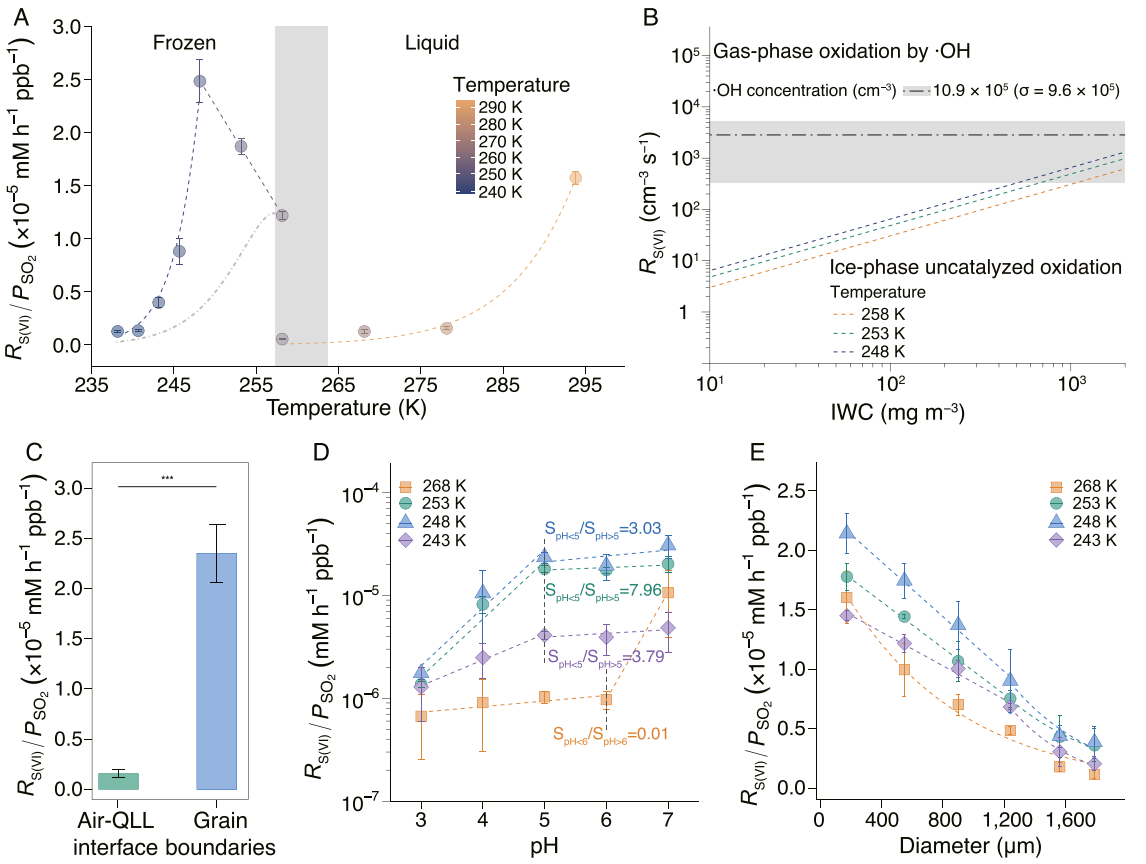

Figure 3. Altered kinetics and their mechanistic origins in frozen microdroplets. (A) Normalized S(VI) formation rates, $R_{S(VI)}/P_{SO_2}$ (where $R_{S(VI)}$ is the formation rate of S(VI) and P_{SO_2} is the partial pressure of gaseous SO_2), varying with temperature. The gray shaded region marks the temperature range of ice nucleation. At 258 K, since the microdroplets were partially frozen, the S(VI) formation rates are determined separately for the liquid and frozen microdroplets. $R_{S(VI)}/P_{SO_2}$ results are independently fitted with the Arrhenius expression for the frozen (238−248 K) and liquid (258−294 K) regimes (short dashed lines), while the gray dot-dashed line depicts the predicted rates in frozen microdroplets based on the theoretical freeze-concentration effect (Text S6 of SI). (B) S(VI) formation by SO_2 conversion in the ice phase and gas phase plotted against IWC (SO_2 mixing ratio: 150 pptv). Colored dashed lines indicate formation rates at different temperatures. The black dot-dashed line represents S(VI) formation rate calculated using the global average concentration of tropospheric hydroxyl radical ($^{\bullet}OH$), with the standard deviation range shown by the gray shaded region. The calculation details were taken from the literature,[45,46] as specified in Text S6 of SI. (C) Comparison of the normalized S(VI) formation rate at the air-QLL interface (the freezing of microdroplets prior to the introduction of SO_2(g)) and the S(VI) formation rate within ice grain boundaries (the introduction of SO_2(g) prior to the freezing of microdroplets). Statistical significance between groups is marked as *** ($p < 0.001$). Error bar represents one standard deviation. (D) Normalized S(VI) formation rates as a function of microdroplet pH at different temperatures (distinguished by symbols with different colors). Short dashed lines indicate piecewise linear fits applied to the data, the ratio of slopes (denoted as S) between adjacent segments listed alongside for each temperature condition. (E) Normalized S(VI) formation rates as a function of microdroplet diameter at different temperatures. The data were fitted linearly for liquid/frozen microdroplets smaller than 1200 μm but exponentially for frozen microdroplets larger than 1200 μm. The experimental methodology and quantification of S(VI) formation rates are detailed in Text S6 of the SI. Error bar represents one standard deviation.

Microdroplet size influences both ice nucleation activity and freezing rate,[1,21] with larger microdroplets exhibiting correspondingly longer freezing time, and ice crystal dendritic growth within them is more readily captured (Figure 1B). Dendritic crystal growth leads to partial solidification, while the solute distribution remains relatively uniform.

Furthermore, quantitative assessment of how temperature and microdroplet size impact ice grain boundaries was achieved by estimating component volume densities via the Delesse principle[22] (Text S3 of SI), which states that the areal fraction of a component in a cross section estimates its volume fraction. We calculated: (i) the grain boundary fraction ($f_{boundaries}$), defined as the number of $\nu_s(SO_4^{2-})$ pixels divided by the total pixel count of the frozen microdroplet ($\cup[\nu_s(SO_4^{2-}), \nu(H_2O)]$); and (ii) the intensity of freeze-concentration ($I_{boundaries}$), indicated by the averaged intensity of $\nu_s(SO_4^{2-})$ at the ice grain boundaries (see Figure 1C).

Continuous cooling progressively elevates $I_{boundaries}$ in ice grain boundaries (Figure S3A), corroborating the trends observed in Figure 1B. Analyzing the temperature dependence of the boundary width reveals that these grain boundaries initially contract as the temperature decreases (Figure S2D). As freezing progresses, the pronounced growth of ice crystals severely compresses specific boundaries, forcing the expulsion of interstitial liquid into adjacent regions and making those boundaries unresolvable for the width analysis (Figure S2E). Consequently, the measurable average width of grain boundaries plateaus at a minimum value, remaining invariant upon further cooling.

After analyzing $f_{boundaries}$ and $I_{boundaries}$ in frozen microdroplets of different diameters, we found that $f_{boundaries}$ is negatively

https://doi.org/10.1021/jacs.6c11450
J. Am. Chem. Soc. 2026, 148, 37134−37143

correlated with microdroplet diameter ($p < 0.01$, Figure 1D), while $I_{boundaries}$ is positively correlated ($p < 0.01$, Figure 1E). That is, smaller frozen microdroplets exhibit a higher fraction of ice grain boundaries but a lower averaged solute concentration, most likely explained by the more rapid freezing of smaller microdroplets producing smaller ice crystals.[23]

Water Structure of Interstitial Liquid and Ice−Water Interface

We analyzed the SRS spectra of $\nu(H_2O)$ for supercooled liquid microdroplets (Figure 2A) and ice grain boundaries within frozen microdroplets (Figure 2B) at the same temperature. When liquid water underwent phase transition to ice Ih (hexagonal water ice), the $\nu(H_2O)$ red-shifted due to the strengthening of hydrogen bonds, and molecular H_2O becomes more fixed in the lattice.[24] In contrast, as shown in Figure 2C, the $\nu(H_2O)$ within ice grain boundary exhibits nonmonotonic shifts. We divided each ice grain boundary into two distinct regions: the ice−water interfaces and the enclosed interstitial liquid (Figure 2B). Near the center of the interstitial liquid, $\nu(H_2O)$ reaches ∼3300 cm^{-1}, which is lower than the 3352 cm^{-1} of supercooled liquid water (Figure 2C), reflecting a stronger hydrogen bonding in the interstitial liquid, distinct from the QLL on premelted ice.[25] This observation is consistent with previous molecular dynamics simulations.[23]

Owing to the finite spatial resolution inherent to spectroscopic methods, the features of ice−water interface are heavily obscured by signals of interstitial liquid and ice Ih. To retrieve the intrinsic interfacial spectrum, we applied multivariate curve resolution with alternating least-squares (MCR-ALS) method to decompose the measured SRS spectrum of ice grain boundary into an interfacial spectrum, an interstitial liquid spectrum, and an ice Ih spectrum (Figure 2D). This approach provides robust interface selectivity within solution.[26] We compared the $\nu(H_2O)$ for three distinct hydrogen-bonding environments: (i) supercooled liquid water, (ii) bulk ice, and (iii) ice−water interface (Figure S12A). At the ice−water interface, we observed blue shifts relative to supercooled liquid water, indicating weakened hydrogen-bonding interactions. Additionally, the characteristic shoulder peak of hydroxyl (OH) stretching associated with strong hydrogen bonding shifted from 3,273 cm^{-1} in supercooled liquid water to 3,331 cm^{-1} at ice−water interface (Figures 2E and S12B). Simultaneously, its fractional peak area decreased from ∼35% of the entire $\nu(H_2O)$ to ∼10%. This likely arises from the interactions among the ice lattice, free water molecules, and solute molecules at the interface, forcing H_2O molecules into configurations distinct from bulk water and disrupting the solvation structure surrounding solutes in the interfacial region.

Our spectroscopic observations indicate that the buried ice−water interface differs from the air−ice interface in water structure, at which undercoordinated surface water molecules form a disordered layer.[27] Instead, the buried ice−water interface more closely resembles the inner region of the QLL, where water molecules remain partially ordered by the underlying ice lattice to lower the surface energy.[28]

Altered Kinetics in Frozen Droplets

To determine whether these anomalous structural features result in altered reactivity, we selected the oxidation of SO_2 as a model reaction. The oxidation products of SO_2, namely S(VI), are key constituents for aerosol formation and growth throughout the troposphere.[29,30] Our experiments revealed a distinct reaction regime within frozen microdroplets (diameter range: 20−200 μm; pH: 5.0). Ice nucleation can be observed within a narrow temperature range (258−264 K) (Figure S1C), enabling a clear distinction between the temperature ranges of the frozen and liquid microdroplets (Figure 3A). In the liquid (258−295 K) microdroplets, the reaction rate normalized by SO_2 partial pressure ($R_{S(VI)}/P_{SO_2}$) followed a standard positive temperature dependence. A similar trend is observed in the lower-temperature frozen microdroplets (238−248 K), whereas an inverse temperature dependence emerges in the higher freezing range of 248−258 K, where the rate increased linearly as temperature dropped. We further compared $R_{S(VI)}$ in ice clouds with those from gas-phase hydroxyl radical ($^{\bullet}OH$) oxidation as a function of ice water content (IWC), which reaches up to 1.5 g m^{-3} in atmospheric convective profiles.[31,32] When IWC exceeds ∼0.5 g m^{-3}, the ice-phase S(VI) formation rate becomes comparable to that of the gas-phase $^{\bullet}OH$ reaction (Figure 3B).

Such acceleration was not observed when SO_2 was exposed to prefrozen microdroplets (Figure 3C), which suggests negligible reactivity at the QLL. The oxidation of S(IV) is thus likely occurring within ice grain boundaries. The differences in reactivity across these interfaces could be attributed to their distinct physicochemical properties. Although the QLL may share a similar water structure with ice grain boundaries, its relatively small pH variation is expected to limit its chemical reactivity.[27]

Mechanistic Origin of the Altered Kinetics

Previous studies attributed the accelerated reactions in ice to the freeze-concentration effect on solutes[33,34] and proposed models for bulk ice.[35−37] We quantified this effect (Figure 3A, depicted by the gray dot-dashed line) and found that the model prediction is 55.1−86.7% lower than our experimental data. To further and more comprehensively elucidate the specific mechanisms driving these accelerated kinetics, we selected three freezing temperatures (243, 248, 253 K) and one liquid phase temperature (268 K) to assess the impact of microdroplet pH, ionic strength (IS), and diameter on $R_{S(VI)}/P_{SO_2}$.

The kinetics in frozen microdroplets are distinct from those in liquid microdroplets. As shown in Figure 3D, the pH dependence of $R_{S(VI)}/P_{SO_2}$ in liquid microdroplets manifests two regimes, respectively controlled by interfacial reaction (pH < 6) and SO_2 solubility (pH > 6).[38] In contrast, this trend is distinctly altered in frozen microdroplets, where $R_{S(VI)}/P_{SO_2}$ is pH-dependent at pH < 5 but becomes pH-independent when pH > 5. Since no transition metal ions (TMIs) or oxidants other than O_2 were introduced, sulfate formation likely proceeds via uncatalyzed oxidation.[39] We tested this hypothesis using electron paramagnetic resonance (EPR, see Text S6 of SI) and detected $SO_3^{\bullet-}$ in frozen microdroplets under both elevated gas-phase mixing ratio of SO_2 (∼7 ppmv) and atmospherically relevant SO_2 conditions (∼68 ppbv) (Figure S6A). Mechanistically, $SO_3^{\bullet-}$ could trigger a series of free-radical propagation steps (eqs S7−S15) to produce S(VI). The initial step involves the interaction between bisulfite ion (HSO_3^-) and O_2 to form $SO_3^{\bullet-}$ alongside $O_2^{\bullet-}$ (eq S7), which is supported by the increased abundance of $O_2^{\bullet-}$ with freezing duration (Figure S6B). Furthermore, triple oxygen isotope measurements imply that the radical chain reaction pathway may involves $SO_3^{\bullet-}$ formation in frozen microdroplets (Figure S6D, Text S7 of SI). Although this process is typically inhibited under neutral liquid conditions,[40] $SO_3^{\bullet-}$ remained detectable in frozen microdroplets even when the original liquid pH was close to 7.0, in contrast to

https://doi.org/10.1021/jacs.6c11450
J. Am. Chem. Soc. 2026, 148, 37134−37143

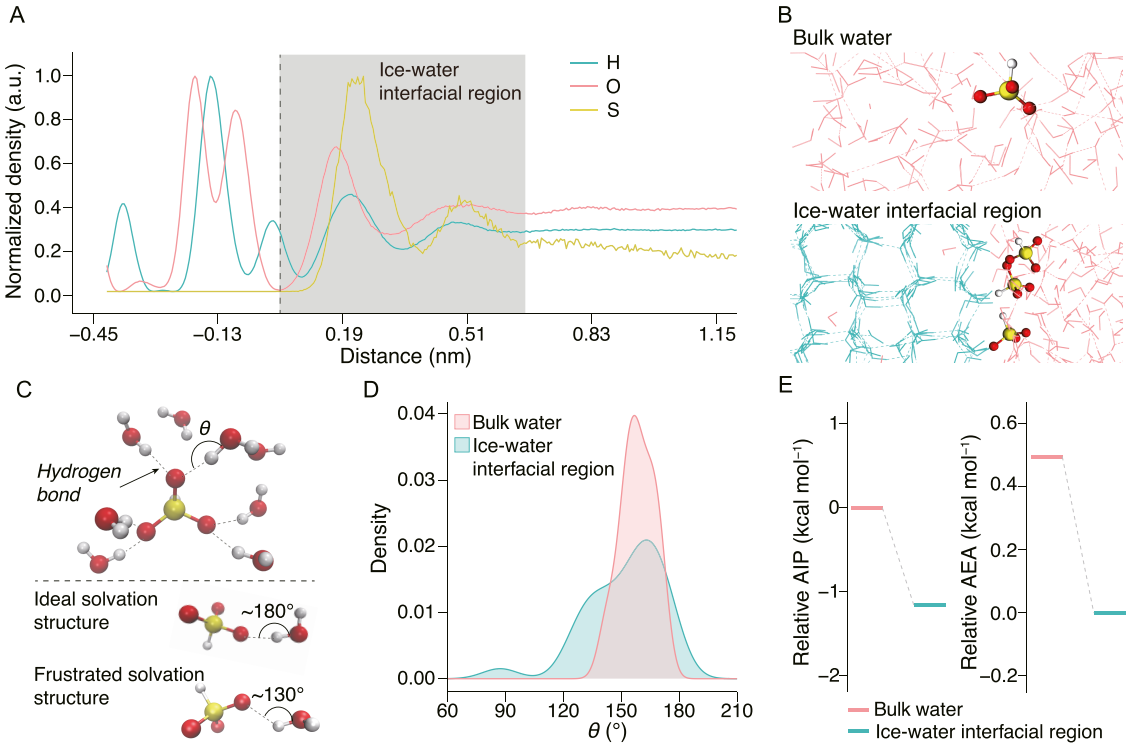

Figure 4. Simulations of ice−water interface. (A) Molecular dynamics (MD) simulation indicating the normalized density profiles of H, O, and S atoms as a function of the distance perpendicular to the ice−water interface orientated by the vertical gray dashed line. The extent of ice−water interfacial region is determined by the Willard-Chandler instantaneous interface method,[51] as shown by the gray shaded area (6.84 ± 2.77 Å). (B) Snapshots of HSO_3^- in bulk water and ice−water interfacial region, simulated by MD. (C) Illustrations of the solvation of HSO_3^- (top). The gray dashed lines represent the hydrogen bond between H_2O and HSO_3^-. The $O_{S(IV)}\cdots H_{water}-O_{water}$ angle (θ_{OHO}) in an ideal solvation structure is greater than that in a frustrated solvation structure (bottom). (D) Histogram plot indicating the density of θ_{OHO} within the first shell of H_2O surrounding HSO_3^- in bulk water and ice−water interfacial region. (E) Relative adiabatic ionization potential (AIP) for HSO_3^- (left) and the relative adiabatic electron affinity (AEA) for O_2 in bulk water and ice−water interfacial region.

liquid microdroplets. Thus, freezing of microdroplets broadens the pH range for the uncatalyzed oxidation of S(IV).

Freezing of microdroplets drives the unequal incorporation of ions into the ice phase,[41] thereby modulating the balance of H_3O^+ and OH^- within ice grain boundaries. We found that the grain boundary pH decreased by about 1.5 units relative to the liquid microdroplet pH (Figure S10, Text S12 of SI). We therefore propose that freezing creates favorable pH conditions for the generation of $SO_3^{\bullet-}$ in microdroplets. This hypothesis is supported by the influence of IS on $R_{S(VI)}/P_{SO_2}$ and pH shift (Figures S7A, 10D−F). In liquid microdroplets, IS enhances the S(VI) formation rate through salt effects on the equilibrium of SO_2 dissolution, and it also elevates the rate constant for S(IV) autoxidation,[38,42] thus causing the increased $R_{S(VI)}/P_{SO_2}$ with IS. In frozen microdroplets, $R_{S(VI)}/P_{SO_2}$ increases with IS at lower IS (<1 mol kg^{-1}); however, further increases in IS counteracted the acidification within ice grain boundaries, causing a rapid decline in $R_{S(VI)}/P_{SO_2}$.

Acidification of ice grain boundaries alone is insufficient to account for the size dependence observed in the S(VI) formation. Reaction kinetics in frozen microdroplets generally exhibit a negative size dependence, qualitatively similar to the trends observed in liquid microdroplets but characterized by different scaling behaviors (see Figure 3E). As for the liquid microdroplets previously studied, uncatalyzed SO_2 autoxidation predominantly occurs on the microdroplet surface, with S(VI) formation depending linearly on the surface-to-volume ratio.[38] In contrast, for frozen microdroplets, the negative correlations ($p < 0.01$) between the frozen microdroplet size and $R_{S(VI)}/P_{SO_2}$ demonstrate that the S(VI) formation is also strongly affected by a diameter-dependent factor.

Differences in microdroplet size may affect both freezing kinetics and microstructures of frozen microdroplets. Given that freezing times among microdroplets of different sizes are several orders of magnitude shorter than the reaction time scale, the observed size dependence of the reaction kinetics is more likely attributable to structure variations in frozen microdroplets. Consistent with this interpretation, SRS imaging reveals that $f_{boundaries}$ increases with a decrease in microdroplet size (Figure 1D). The resulting increase in $f_{boundaries}$ therefore accounts for the size-dependent $R_{S(VI)}/P_{SO_2}$ values observed in frozen microdroplets. This can be supported by the positive correlations between $R_{S(VI)}/P_{SO_2}$ and $f_{boundaries}$ for frozen microdroplets at diverse temperatures (Figure S3C). Consequently, a larger fraction of grain boundaries is associated with a more rapid S(VI) formation.

In contrast to the robust hydrogen bond network of the interstitial liquid, the frustrated hydrogen bonding at the ice−water interface is more likely to facilitate electron transfer from HSO_3^- to an electron acceptor.[16,43] We conducted a variance-based sensitivity analysis to assess the relative contributions of the ice−water interfacial effect to the $R_{S(VI)}/P_{SO_2}$ in frozen microdroplets.[44] The results indicate that the relative contributions of IS (2.2%) and pH (6.0%) to the enhanced sulfate

https://doi.org/10.1021/jacs.6c11450
J. Am. Chem. Soc. 2026, 148, 37134−37143

formation under frozen conditions are substantially smaller than those of temperature (91.7%). Because decreasing temperature simultaneously affects the apparent reaction rate constant, the freeze-concentration factor, and $f_{boundaries}$, the overall temperature effect can be further separated into contributions from freeze-concentration and the interfacial effect. As shown in Figure 3A, the freeze-concentration effect accounts for less than 50% of the observed enhancement in sulfate formation associated with decreasing temperature. These results suggest that the ice−water interfacial effect is likely to contribute substantially to the accelerated sulfate formation and may play a more important role than either ionic-strength effects or proton activity effects. When considered together with the previous spectroscopic results, the sensitivity analysis provides converging support for the proposed reaction mechanism involving the ice−water interfacial effect.

To investigate the molecular origins of this interfacial frustration and its mechanistic impact on reaction kinetics, we conducted classical molecular dynamics (MD) simulations of an ice grain boundary and bisulfite (HSO_3^-) ions and O_2 within it. The densities of solvent O and H atoms, together with the solute S atoms, were profiled as a function of the distance perpendicular to the ice−water interface (Figure 4A, Text S12 of SI). The structural and dynamic properties of the ice−water interface affect the H_2O molecules and solutes nearby.[15] A previous study has shown that the ice lattice can prolong the hydrogen bond lifetime of nearby water molecules by up to 13-fold.[23] In contrast, we found that the hydrogen bond lifetime within the first solvation shell of the solutes in the ice−water interfacial region was comparable to that in bulk water (17.2 ps), indicating that the slowdown of solvation dynamics imposed by the ice lattice is reduced in the ice−water interfacial region. We further calculated the average tetrahedral order parameter ($\overline{q}_4$) in the presence of the solutes. The interfacial region exhibited a lower $\overline{q}_4$ (0.5) than that of bulk water (0.6), revealing a reduced structural ordering of water molecules surrounding the solutes in the ice−water interfacial region, consistent with the SRS measurements. After simulation, the snapshots of HSO_3^- in liquid water and the ice−water interfacial region are shown in Figure 4B. To obtain a more accurate description of the molecular structure, we performed ab initio molecular dynamics (AIMD) simulations of HSO_3^- at the ice−water interfacial region and bulk water. No significant differences in the S−O bond lengths or O−S−O bond angles of HSO_3^- were observed between the two environments (Figure S12C), suggesting that confinement at the ice−water interface has little influence on the molecular geometry of HSO_3^-. In contrast, the radial distribution function (RDF) and coordination number (CN) for interactions of HSO_3^- and O_2 with H_2O were analyzed. Both HSO_3^- and O_2 in the interfacial region exhibit a lower CN (Figure S12D,E), indicating weaker coordination.

For the ideal solvation structure of HSO_3^-, the hydrogen atoms of H_2O experience an attractive potential from oxygen atoms of HSO_3^- and tend to form hydrogen bonds (Figure 4C, top panel). The closer the $O_{S(IV)}\cdots H_{water}-O_{water}$ angle (θ_{OHO}) is to 180°, the stronger the interactions would be.[47] Here, we statistically analyzed the θ_{OHO} within the first solvation shell of HSO_3^- and found that the distribution of θ_{OHO} in ice−water interfacial region is broader than that in bulk water (Figure 4D). The variation in θ_{OHO} in the interfacial region mainly arises from frustration (Figure 4C, bottom panel, the structural order of the hydrogen bond network is frustrated), where the highly ordered ice Ih surface imposes orientational constraints on the surrounding H_2O molecules. Frustration is known to influence energy gap fluctuations,[48] and is critical in solvent-mediated electron transfer.[49] Specifically, for HSO_3^- in the confined interfacial region, the partial desolvation relative to the bulk creates significant frustration, accompanied by enhanced fluctuations and accelerated electron-transfer rates.[16,43,50] Our quantum chemical calculations corroborate this mechanistic hypothesis. Specifically, the adiabatic ionization potential (AIP) for HSO_3^- and the adiabatic electron affinity (AEA) for O_2 are reduced by 1.2 and 0.5 kcal mol^{-1}, respectively (Figure 4E), within ice−water interfacial region relative to bulk water. Concurrently, the reorganization energy for this electron-transfer reaction decreases by 38.3%. These results support an electron-transfer-favoring effect of ice−water interfacial region. In summary, freezing of microdroplet drives the exclusion of solutes into acidified grain boundaries, lowering the activation energy for $SO_3^{\bullet-}$ generation, while the frustrated solvation structure at the ice−water interface enhances electron-transfer rates, collectively accelerating S(VI) formation.

CONCLUSION

The complex dynamics of microdroplet freezing generates intricate internal microstructures. By employing SRS imaging and spectral analysis, the temperature-dependent evolution of polycrystalline ice at the microdroplet scale is clearly resolved. Using the autoxidation of SO_2 as a model system, we integrated SRS spectroscopic analysis with kinetic experiments and theoretical calculations to elucidate the mechanistic origins of the altered kinetics in frozen microdroplets. Freezing segregates dissolved S(IV) into acidified ice grain boundary within polycrystalline ice. These interstitial liquids exhibit heterogeneous water structures, including strongly hydrogen-bonded interstitial water and frustrated solvation at buried ice−water interfaces. The reduced electron-transfer energy barrier and enhanced sulfite-derived radical formation are associated with interfacial partial desolvation within the acidified grain boundaries. These effects are consistent with the enhanced S(VI) formation in frozen microdroplets beyond what is expected from freeze-concentration alone. These findings provide a microscopic framework for understanding how buried ice−water interfaces and grain boundary chemistry regulate low-temperature multiphase reactions. The proposed mechanism may also operate in acidified QLL, with implications for the formation of sulfate and other pollutants in cold and mixed-phase atmospheric environments.

ASSOCIATED CONTENT

Supporting Information

The Supporting Information is available free of charge at https://pubs.acs.org/doi/10.1021/jacs.6c11450.

Chemicals, heterogeneous ice nucleation measurement, cryogenic stimulated Raman imaging and analyses, kinetic experimental details, quantification of S(VI) formation rate, detection of free radicals, sulfate triple oxygen isotope measurement, the effect of temperature on S(IV) equilibria, fabrication and characterization of surface-enhanced Raman scattering (SERS) pH probe, identification of the grain boundaries, estimating pH at the grain boundaries, and computational details (PDF)

https://doi.org/10.1021/jacs.6c11450
J. Am. Chem. Soc. 2026, 148, 37134−37143

AUTHOR INFORMATION

Corresponding Authors

Tao Wang − *Shanghai Key Laboratory of Air Quality and Environmental Health, Department of Environmental Science and Engineering, Fudan University, Shanghai 200433, People's Republic of China; Shanghai Institute of Pollution Control and Ecological Security, Shanghai 200092, People's Republic of China;* orcid.org/0000-0001-9137-5243; Email: wangtao_fd@fudan.edu.cn

Minbiao Ji − *State Key Laboratory of Surface Physics and Department of Physics, Fudan University, Shanghai 200092, People's Republic of China*; Email: minbiaoj@fudan.edu.cn

Liwu Zhang − *Shanghai Key Laboratory of Air Quality and Environmental Health, Department of Environmental Science and Engineering, Fudan University, Shanghai 200433, People's Republic of China; Shanghai Institute of Pollution Control and Ecological Security, Shanghai 200092, People's Republic of China;* orcid.org/0000-0002-0765-8660; Email: zhanglw@fudan.edu.cn

Zhang Lin − *School of Metallurgy and Environment, Central South University, Changsha 410083, People's Republic of China;* orcid.org/0000-0002-6600-2055; Email: zhang_lin@csu.edu.cn

Authors

Runbo Wang − *Shanghai Key Laboratory of Air Quality and Environmental Health, Department of Environmental Science and Engineering, Fudan University, Shanghai 200433, People's Republic of China; School of Metallurgy and Environment, Central South University, Changsha 410083, People's Republic of China*

Kuan Luo − *State Key Laboratory of Surface Physics and Department of Physics, Fudan University, Shanghai 200092, People's Republic of China;* orcid.org/0009-0001-2661-1577

Yu Wei − *International Center for Isotope Effects Research, State Key Laboratory of Critical Earth Material Cycling and Mineral Deposits, Nanjing University, Nanjing 210023, People's Republic of China;* orcid.org/0000-0002-9409-8656

Jilun Wang − *Shanghai Key Laboratory of Air Quality and Environmental Health, Department of Environmental Science and Engineering, Fudan University, Shanghai 200433, People's Republic of China*

Le Yang − *Shanghai Key Laboratory of Air Quality and Environmental Health, Department of Environmental Science and Engineering, Fudan University, Shanghai 200433, People's Republic of China*

Wenbo You − *Shanghai Key Laboratory of Air Quality and Environmental Health, Department of Environmental Science and Engineering, Fudan University, Shanghai 200433, People's Republic of China*

Qiuyue Ge − *Shanghai Key Laboratory of Air Quality and Environmental Health, Department of Environmental Science and Engineering, Fudan University, Shanghai 200433, People's Republic of China*

Yangyang Liu − *Shanghai Key Laboratory of Air Quality and Environmental Health, Department of Environmental Science and Engineering, Fudan University, Shanghai 200433, People's Republic of China;* orcid.org/0000-0001-5118-4901

Minglu Ma − *Shanghai Key Laboratory of Air Quality and Environmental Health, Department of Environmental Science and Engineering, Fudan University, Shanghai 200433, People's Republic of China*

Kejian Li − *Shanghai Key Laboratory of Air Quality and Environmental Health, Department of Environmental Science and Engineering, Fudan University, Shanghai 200433, People's Republic of China*

Yuting Lyu − *Universite Claude Bernard Lyon 1, CNRS, IRCELYON, Villeurbanne F-69100, France;* orcid.org/0000-0001-9746-4466

Laurentiu-Gabriel Movila − *Universite Claude Bernard Lyon 1, CNRS, IRCELYON, Villeurbanne F-69100, France*

Xiang Sun − *International Center for Isotope Effects Research, State Key Laboratory of Critical Earth Material Cycling and Mineral Deposits, Nanjing University, Nanjing 210023, People's Republic of China;* orcid.org/0000-0001-7693-1125

Huiming Bao − *International Center for Isotope Effects Research, State Key Laboratory of Critical Earth Material Cycling and Mineral Deposits, Nanjing University, Nanjing 210023, People's Republic of China;* orcid.org/0000-0002-1979-4395

Jianmin Chen − *Shanghai Key Laboratory of Air Quality and Environmental Health, Department of Environmental Science and Engineering, Fudan University, Shanghai 200433, People's Republic of China;* orcid.org/0000-0001-5859-3070

Christian George − *Universite Claude Bernard Lyon 1, CNRS, IRCELYON, Villeurbanne F-69100, France;* orcid.org/0000-0003-1578-7056

Norimichi Takenaka − *Graduate School of Sustainable System Sciences, Osaka Metropolitan University, Sakai−shi, Osaka 599−8531, Japan*

Markku Kulmala − *University of Helsinki, Faculty of Science, Institute for Atmospheric and Earth System Research(INAR)/ Physics, University of Helsinki, Helsinki FIN-00014, Finland;* orcid.org/0000-0003-3464-7825

Complete contact information is available at: https://pubs.acs.org/10.1021/jacs.6c11450

Author Contributions

◆R.W. and K.L. contributed equally to this work. The manuscript was written through contributions of all authors. All authors have given approval to the final version of the manuscript.

Funding

The authors gratefully acknowledge financial support from National Natural Science Foundation of China (grant Nos. 22494680, W2521189, 22494684, 22376028, 62425501, and 22576036).

Notes

The authors declare no competing financial interest.

ACKNOWLEDGMENTS

The computations in this work were performed using the CFFF platform of Fudan University.

REFERENCES

(1) Kalita, A.; Mrozek-McCourt, M.; Kaldawi, T. F.; Willmott, P. R.; Loh, N. D.; Marte, S.; Sierra, R. G.; Laksmono, H.; Koglin, J. E.; Hayes,

M. J.; Paul, R. H.; Guillet, S. A. H.; Aquila, A. L.; Liang, M. N.; Boutet, S.; Stan, C. A. Microstructure and crystal order during freezing of supercooled water drops. *Nature* **2023**, *620* (7974), 557−561.
(2) Bogdan, A.; Molina, M. J.; Tenhu, H.; Mayer, E.; Loerting, T. Formation of mixed-phase particles during the freezing of polar stratospheric ice clouds. *Nat. Chem.* **2010**, *2* (3), 197−201.
(3) Murray, K. A.; Gibson, M. I. Chemical approaches to cryopreservation. *Nat. Rev. Chem.* **2022**, *6* (8), 579−593.
(4) Kreder, M. J.; Alvarenga, J.; Kim, P.; Aizenberg, J. Design of anti-icing surfaces: smooth, textured or slippery? *Nat. Rev. Mater.* **2016**, *1* (1), No. 15003.
(5) Bartels-Rausch, T.; Jacobi, H. W.; Kahan, T. F.; Thomas, J. L.; Thomson, E. S.; Abbatt, J. P. D.; Ammann, M.; Blackford, J. R.; Bluhm, H.; Boxe, C.; Domine, F.; Frey, M. M.; Gladich, I.; Guzmán, M. I.; Heger, D.; Huthwelker, T.; Klán, P.; Kuhs, W. F.; Kuo, M. H.; Maus, S.; Moussa, S. G.; McNeill, V. F.; Newberg, J. T.; Pettersson, J. B. C.; Roeselová, M.; Sodeau, J. R. A review of air-ice chemical and physical interactions (AICI): liquids, quasi-liquids, and solids in snow. *Atmos. Chem. Phys.* **2014**, *14* (3), 1587−1633.
(6) Luo, T.; Chen, T.; Bui Thi, T. M.; Behan, J.; Hetherington, C.; Hanna, K.; Boily, J.-F. A single freeze cycle redirects iron mineral transformation. *Science* **2026**, *393* (6807), 212−216.
(7) Schohn, C. M.; Iverson, N. R.; Zoet, L. K.; Fowler, J. R.; Morgan-Witts, N. Linear-viscous flow of temperate ice. *Science* **2025**, *387* (6730), 182−185.
(8) Wen, X.; Ma, Q.; Liu, J.; Saeed, U.; Shen, S.; Catalan, G. Streaming flexoelectricity in saline ice. *Nat. Mater.* **2025**, *24* (10), 1533−1537.
(9) Kauffmann, P. J.; Blanco-Combariza, C. A.; Dick, J. E. Witnessing a discrete microdroplet freezing event via real-time electrochemical monitoring of solution temperature. *Analyst* **2025**, *150* (2), 386−394.
(10) Vanoss, C. J.; Giese, R. F.; Wentzek, R.; Norris, J.; Chuvilin, E. M. Surface tension parameters of ice obtained from contact angle data and from positive and negative particle adhesion to advancing freezing fronts. *Adhes. Sci. Technol.* **1992**, *6* (4), 503−516.
(11) Lee, A. J.; Rick, S. W. Characterizing charge transfer at water ice interfaces. *J. Phys. Chem. Lett.* **2012**, *3* (21), 3199−3203.
(12) Daigle, H. Structure of the electrical double layer at the ice-water interface. *J. Chem. Phys.* **2021**, *154* (21), No. 214703.
(13) Sebaaly, A. P.; van Rijn, F.; Hanna, K.; Boily, J. F. Ice as a kinetic and mechanistic driver of oxalate- promoted iron oxyhydroxide dissolution. *Proc. Natl. Acad. Sci. U.S.A.* **2025**, *122* (35), No. e2507588122.
(14) Shi, Y. F.; Xiao, S. Z.; Zhou, X. F.; Qian, Y. J.; Zhao, Q. P.; Xing, M. Y.; Jiang, Y.; Wang, T. R.; Liu, T. C.; Li, N.; Zhang, Y. L.; Chen, J. B. Spatial Ice Confinement Enabled Chemical Reaction Acceleration for Water Purification. *Environ. Sci. Technol.* **2026**, *60* (14), 11124−11134.
(15) Wan, S.-P.; Wang, D.; Wu, J.; Zhang, S.; Chen, X.; Zhang, C.; Liu, J.; Zhou, X.; He, Z.; Wang, J. Inhibiting Isomerization via Confinement in Ice-Water Interfaces Enhances Stereoselectivity in [2 + 2] Cycloaddition. *J. Am. Chem. Soc.* **2025**, *147* (41), 37290−37298.
(16) Remsing, R. C.; McKendry, I. G.; Strongin, D. R.; Klein, M. L.; Zdilla, M. J. Frustrated solvation structures can enhance electron transfer rates. *J. Phys. Chem. Lett.* **2015**, *6* (23), 4804−4808.
(17) Campbell, J. R.; Battaglia, M., Jr.; Dingilian, K.; Cesler-Maloney, M.; Simpson, W.; Robinson, E.; DeCarlo, P.; Temime-Roussel, B.; D'Anna, B.; Holen, A.; Wu, J.; Pratt, K.; Dibb, J.; Nenes, A.; Weber, R.; Mao, J. Enhanced aqueous formation and neutralization of fine atmospheric particles driven by extreme cold. *Sci. Adv.* **2024**, *10* (36), No. eado4373.
(18) Cheng, Y.; He, K. Northeast China: an emerging hotspot of atmospheric sciences. *Sci. Bull.* **2026**, *71* (1), 64−66.
(19) Zhang, Q.; Li, R.; Li, W.; Li, X.; Ng, C.; Zhang, S.; Zhao, C. Climate impacts and future trends of hailstorms in China based on millennial records. *Nat. Commun.* **2025**, *16* (1), No. 8000.
(20) Gao, J.; Wang, H.; Liu, W.; Xu, H.; Wei, Y.; Tian, X.; Feng, Y.; Song, S.; Shi, G. Hydrogen peroxide serves as pivotal fountainhead for aerosol aqueous sulfate formation from a global perspective. *Nat. Commun.* **2024**, *15* (1), No. 4625.
(21) Duft, D.; Leisner, T. Laboratory evidence for volume-dominated nucleation of ice in supercooled water microdroplets. *Atmos. Chem. Phys.* **2004**, *4*, 1997−2000.
(22) Mayhew, T. M.; Orive, L. M. C. Caveat on the use of the Delesse principle of areal analysis for estimating component volume densities. *J. Microsc.* **1974**, *102* (2), 195−207.
(23) Arsiccio, A.; McCarty, J.; Pisano, R.; Shea, J. E. Heightened cold-denaturation of proteins at the ice-water interface. *J. Am. Chem. Soc.* **2020**, *142* (12), 5722−5730.
(24) Chen, Y.; Liu, Z.; Ji, M. Imaging low-temperature phases of ice with polarization-resolved hyperspectral stimulated Raman scattering microscopy. *J. Phys. Chem. B* **2023**, *127* (11), 2609−2616.
(25) Kahan, T. F.; Reid, J.; Donaldson, D. Spectroscopic probes of the quasi-liquid layer on ice. *J. Phys. Chem. A* **2007**, *111* (43), 11006−11012.
(26) Shi, L.; LaCour, R. A.; Qian, N.; Heindel, J. P.; Lang, X.; Zhao, R.; Head-Gordon, T.; Min, W. Water structure and electric fields at the interface of oil droplets. *Nature* **2025**, *640* (8057), 87−93.
(27) Slater, B.; Michaelides, A. Surface premelting of water ice. *Nat. Rev. Chem.* **2019**, *3* (3), 172−188.
(28) Stranski, I. N. Über den Schmelzvorgang bei nichtpolaren Kristallen. *Naturwissenschaften* **1942**, *30* (28), 425−433.
(29) Yao, L.; Garmash, O.; Bianchi, F.; Zheng, J.; Yan, C.; Kontkanen, J.; Junninen, H.; Mazon, S. B.; Ehn, M.; Paasonen, P.; Sipilä, M.; Wang, M.; Wang, X.; Xiao, S.; Chen, H.; Lu, Y.; Zhang, B.; Wang, D.; Fu, Q.; Geng, F.; Li, L.; Wang, H.; Qiao, L.; Yang, X.; Chen, J.; Kerminen, V. M.; Petäjä, T.; Worsnop, D. R.; Kulmala, M.; Wang, L. Atmospheric new particle formation from sulfuric acid and amines in a Chinese megacity. *Science* **2018**, *361* (6399), 278−281.
(30) Dunne, E. M.; Gordon, H.; Kürten, A.; Almeida, J.; Duplissy, J.; Williamson, C.; Ortega, I. K.; Pringle, K. J.; Adamov, A.; Baltensperger, U.; Barmet, P.; Benduhn, F.; Bianchi, F.; Breitenlechner, M.; Clarke, A.; Curtius, J.; Dommen, J.; Donahue, N. M.; Ehrhart, S.; Flagan, R. C.; Franchin, A.; Guida, R.; Hakala, J.; Hansel, A.; Heinritzi, M.; Jokinen, T.; Kangasluoma, J.; Kirkby, J.; Kulmala, M.; Kupc, A.; Lawler, M. J.; Lehtipalo, K.; Makhmutov, V.; Mann, G.; Mathot, S.; Merikanto, J.; Miettinen, P.; Nenes, A.; Onnela, A.; Rap, A.; Reddington, C. L. S.; Riccobono, F.; Richards, N. A. D.; Rissanen, M. P.; Rondo, L.; Sarnela, N.; Schobesberger, S.; Sengupta, K.; Simon, M.; Sipiläa, M.; Smith, J. N.; Stozkhov, Y.; Tomé, A.; Tröstl, J.; Wagner, P. E.; Wimmer, D.; Winkler, P. M.; Worsnop, D. R.; Carslaw, K. S. Global atmospheric particle formation from CERN CLOUD measurements. *Science* **2016**, *354* (6316), 1119−1124.
(31) Protat, A.; Delanoë, J.; Strapp, J. W.; Fontaine, E.; Leroy, D.; Schwarzenboeck, A.; Lilie, L.; Davison, C.; Dezitter, F.; Grandin, A.; Weber, M. The measured relationship between ice water content and cloud radar reflectivity in tropical convective clouds. *J. Appl. Meteorol. Clim.* **2016**, *55* (8), 1707−1729.
(32) Reichardt, J.; Knist, C.; Kouremeti, N.; Kitchin, W.; Plakhotnik, T. Accurate absolute measurements of liquid water content (LWC) and ice water content (IWC) of clouds and precipitation with spectrometric water Raman lidar. *J. Atmos. Ocean. Technol.* **2022**, *39* (2), 163−180.
(33) Sun, M.; Gao, D.; Li, B.; Francisco, J. S.; Bai, G.; Zhang, X. Freezing enhances CO_2 mineralization in Ca^{2+}-containing solutions. *Proc. Natl. Acad. Sci. U.S.A.* **2025**, *122* (41), No. e2512544122.
(34) Wu, Y.; Wang, H.; Du, J.; Hu, Y.; Wu, Q.; Guo, W.; Choi, W. Simultaneous oxidation of bromide and dissolution of manganese oxide induced by freezing. *Environ. Sci. Technol.* **2024**, *58* (40), 17948−17958.
(35) Cho, H.; Shepson, P. B.; Barrie, L. A.; Cowin, J. P.; Zaveri, R. NMR investigation of the quasi-brine layer in ice/brine mixtures. *J. Phys. Chem. B* **2002**, *106* (43), 11226−11232.
(36) Takenaka, N.; Bandow, H. Chemical kinetics of reactions in the unfrozen solution of ice. *J. Phys. Chem. A* **2007**, *111* (36), 8780−8786.
(37) Boxe, C. S.; Saiz-Lopez, A. Multiphase modeling of nitrate photochemistry in the quasi-liquid layer (QLL): implications for NOx release from the Arctic and coastal Antarctic snowpack. *Atmos. Chem. Phys.* **2008**, *8* (16), 4855−4864.

(38) Chen, Z.; Liu, P.; Wang, W.; Cao, X.; Liu, Y.; Zhang, Y.; Ge, M. Rapid sulfate formation via uncatalyzed autoxidation of sulfur dioxide in aerosol microdroplets. *Environ. Sci. Technol.* **2022**, *56* (12), 7637−7646.
(39) Hung, H.-M.; Hoffmann, M. R. Oxidation of gas-phase SO_2 on the surfaces of acidic microdroplets: Implications for sulfate and sulfate radical anion formation in the atmospheric liquid phase. *Environ. Sci. Technol.* **2015**, *49* (23), 13768−13776.
(40) Hegg, D. A.; Hobbs, P. V. Oxidation of sulfur dioxide in aqueous systems with particular reference to the atmosphere. *Atmos. Environ.* **1978**, *12* (1−3), 241−253.
(41) Bronshteyn, V. L.; Chernov, A. A. Freezing potentials arising on solidification of dilute aqueous solutions of electrolytes. *J. Cryst. Growth* **1991**, *112* (1), 129−145.
(42) Liu, T.; Clegg, S. L.; Abbatt, J. P. Fast oxidation of sulfur dioxide by hydrogen peroxide in deliquesced aerosol particles. *Proc. Natl. Acad. Sci. U.S.A.* **2020**, *117* (3), 1354−1359.
(43) Li, Z.; Jeanmairet, G.; Méndez-Morales, T.; Burbano, M.; Haefele, M.; Salanne, M. Confinement effects on an electron transfer reaction in nanoporous carbon electrodes. *J. Phys. Chem. Lett.* **2017**, *8* (9), 1925−1931.
(44) Wagner, H. M. Global sensitivity analysis. *Oper. Res.* **1995**, *43* (6), 948−969.
(45) Li, M.; Karu, E.; Brenninkmeijer, C.; Fischer, H.; Lelieveld, J.; Williams, J. Tropospheric OH and stratospheric OH and Cl concentrations determined from CH_4, CH_3Cl, and SF_6 measurements. *npj Clim. Atmos. Sci.* **2018**, *1* (1), No. 29.
(46) Seinfeld, J. H.; Pandis, S. N. *Atmospheric Chemistry and Physics: From Air Pollution to Climate Change*; John Wiley & Sons, 2016.
(47) Arunan, E.; Desiraju, G. R.; Klein, R. A.; Sadlej, J.; Scheiner, S.; Alkorta, I.; Clary, D. C.; Crabtree, R. H.; Dannenberg, J. J.; Hobza, P.; Kjaergaard, H. G.; Legon, A. C.; Mennucci, B.; Nesbitt, D. J. Defining the hydrogen bond: An account (IUPAC Technical Report). *Pure Appl. Chem.* **2011**, *83* (8), 1619−1636.
(48) Blumberger, J. Cu_{aq}^{+}/Cu_{aq}^{2+} redox reaction exhibits strong nonlinear solvent response due to change in coordination number. *J. Am. Chem. Soc.* **2008**, *130* (47), 16065−16068.
(49) Bragg, A. E.; Cavanagh, M. C.; Schwartz, B. J. Linear response breakdown in solvation dynamics induced by atomic electron-transfer reactions. *Science* **2008**, *321* (5897), 1817−1822.
(50) Yang, S.-Y.; Wang, W.; Chen, J.; Francisco, J. S.; Liu, X. Probing catalyst-free hydroxyl radical generation at microbubble interfaces. *Nat. Commun.* **2025**, *16* (1), No. 8835.
(51) Willard, A. P.; Chandler, D. Instantaneous liquid interfaces. *J. Phys. Chem. B* **2010**, *114* (5), 1954−1958.

https://doi.org/10.1021/jacs.6c11450
J. Am. Chem. Soc. 2026, 148, 37134−37143